Coastal Engineering 58 (2011) 510–516

Contents lists available at ScienceDirect

Coastal Engineering

journal homepage: www.elsevier.com/locate/coastaleng

SWAN predictions of waves observed in shallow water onshore of complex bathymetry

L. Gorrell [a,*], B. Raubenheimer [a], Steve Elgar [a], R.T. Guza [b]

[a] Woods Hole Oceanographic Institution, Woods Hole, MA 02543, USA
[b] Scripps Institution of Oceanography, La Jolla, CA 92093, USA

ARTICLE INFO

Article history:
Received 3 August 2010
Received in revised form 10 January 2011
Accepted 20 January 2011
Available online 19 February 2011

Keywords:
Waves
Modeling
Refraction

ABSTRACT

SWAN model predictions, initialized with directional wave buoy observations in 550-m water depth offshore of a steep, submarine canyon, are compared with wave observations in 5.0-, 2.5-, and 1.0-m water depths. Although the model assumptions include small bottom slopes, the alongshore variations of the nearshore wave field caused by refraction over the steep canyon are predicted well over the 50 days of observations. For example, in 2.5-m water depth, the observed and predicted wave heights vary by up to a factor of 4 over about 1000 m alongshore, and wave directions vary by up to about 10°, sometimes changing from south to north of shore normal. Root-mean-square errors of the predicted wave heights, mean directions, periods, and radiation stresses (less than 0.13 m, 5°, 1 s, and 0.05 m^3/s^2 respectively) are similar near and far from the canyon. Squared correlations between the observed and predicted wave heights usually are greater than 0.8 in all water depths. However, the correlations for mean directions and radiation stresses decrease with decreasing water depth as waves refract and become normally incident. Although mean wave properties observed in shallow water are predicted accurately, nonlinear energy transfers from near-resonant triads are not modeled well, and the observed and predicted wave energy spectra can differ significantly at frequencies greater than the spectral peak, especially for narrow-band swell.

1. Introduction

Surface gravity waves propagating across shallow coastal areas are affected by topography (shoaling, refraction, trapping, diffraction, and reflection), nonlinear wave–wave interactions (triad and quartet resonances), and dissipation (wave breaking and bottom friction). The observed evolution of non-breaking waves on narrow, bathymetrically simple shelves is predicted accurately in intermediate water depths by linear wave propagation models (Longuet-Higgins, 1957; Le Méhauté and Wang, 1982; Dalrymple et al., 1984; Panchang et al., 1991; Kirby and Dalrymple, 1994). In shallower nearshore waters, near-resonant spectral energy transfers (described accurately by Boussinesq models) change the shape of the wave energy (frequency) spectrum prior to breaking (Peregrine, 1967; Madsen and Warren, 1984; Freilich and Guza, 1984; Liu et al., 1985; Elgar and Guza, 1985a; Elgar et al., 1990; Madsen et al., 1991; Madsen and Sorensen, 1992; Kaihatu and Kirby, 1995; Herbers and Burton, 1997; Norheim et al., 1998). Breaking wave evolution on alongshore-homogeneous bathymetry has been simulated with linear and nonlinear models by incorporating dissipation terms that are tuned with observations (Battjes and Janssen, 1978; Thornton and Guza, 1983; Battjes and Stive, 1985; Mase and Kirby, 1992; Schaffer et al., 1993; Chen et al., 1997; Chawla et al., 1998; Booij et al., 1999; Apotsos et al., 2008a).

Wave propagation on beaches with alongshore-inhomogeneous bathymetry is more complicated. For example, curved sand bars (Lippmann and Holman, 1990) and rip channels in the surf zone (MacMahan et al., 2006), both with alongshore length scales of order 100 m, cause alongshore variations in wave heights and directions. Large alongshore gradients in surfzone waves, setup, and circulation also can be caused by irregular bathymetry, such as submarine canyons, in water depths as great as 200 m (Long and Özkan-Haller, 2005; Apotsos et al., 2008b).

Wave propagation over complex shelf topography usually is modeled with refraction or refraction–diffraction models (O'Reilly and Guza, 1991; Kirby and Dalrymple, 1994). The third generation wave model Simulating WAves Nearshore (SWAN) has been used extensively to model waves in coastal regions with gradual bathymetric variations (Booij et al., 1999; Ris et al., 1999; Zubier et al., 2003), and to examine the effects of offshore islands (Rogers et al., 2007) on waves in intermediate depths. Model predictions of wave energy spectra in 20- to 120-m water depth along the axis of a submarine canyon are not degraded significantly by the assumption in SWAN that reflection and scattering (Mei, 1989; Thomson et al., 2007) are negligible (Magne et al., 2007). However, the accuracy of SWAN near and in the surf zone, where nonlinearities may be important and where predicted wave directions often are used to drive circulation models (Long and Özkan-Haller,

* Corresponding author at: 266 Woods Hole Road, Woods Hole, MA, 02543, USA. Tel.: +1 508 289 3757; fax: +1 508 457 2194.
E-mail address: lgorrell@whoi.edu (L. Gorrell).

0378-3839/$ – see front matter © 2011 Elsevier B.V. All rights reserved.
doi:10.1016/j.coastaleng.2011.01.013

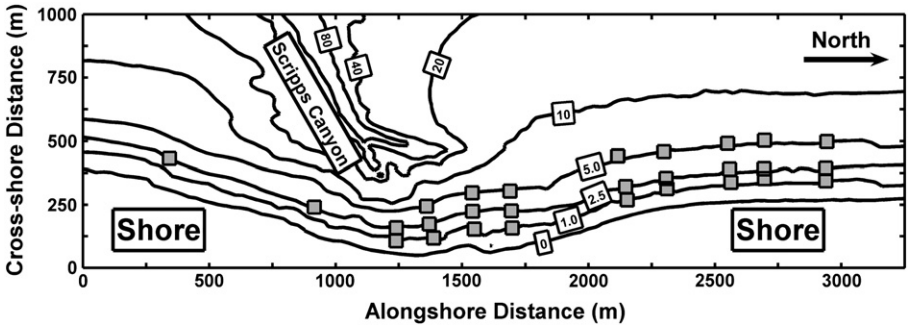

Fig. 1. Locations of colocated current meters and pressure sensors (squares). Curves are depth contours from 0 to 80 m below mean sea level.

2005), is unknown. Here, SWAN model predictions of wave heights, directions, periods, spectra, and radiation stresses onshore of a steep submarine canyon are evaluated by comparison with observations of waves made between 5- and 1-m water depths for a range of incident wave conditions.

2. Observations

Incident wave frequency-directional spectra (a mean direction and spread at each frequency band between 0.05 and 1.00 Hz) were estimated (Kuik et al., 1988) from measurements made with a directional wave buoy (operated and maintained by the Coastal Data Information Program) located about 11 km west (offshore) of the study site in 550-m water depth.

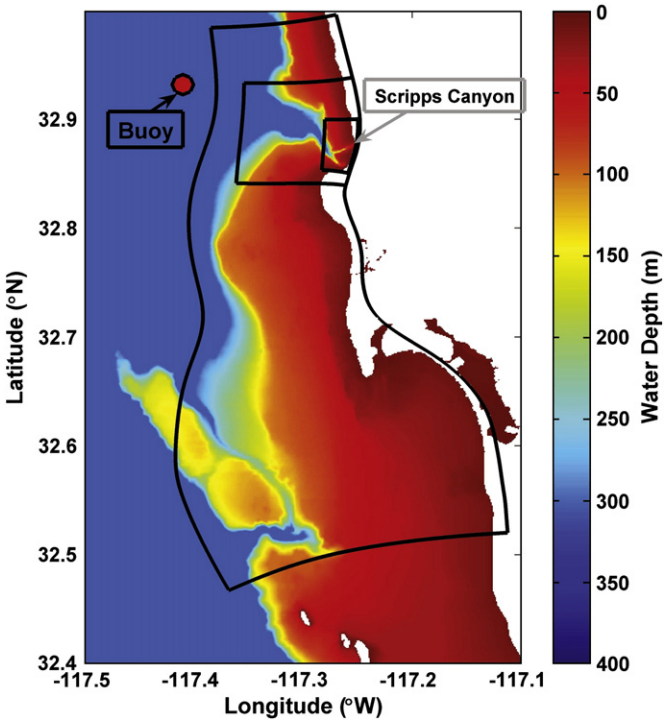

Fig. 2. Nested grids used in the SWAN model runs. Color contours are water depth (scale on the right). Scripps Canyon (Fig. 1) is indicated with an arrow. The three grid sizes (and spatial resolutions) are: small grid: ~5 km alongshore by 3 km cross-shore (resolution between 30 m at the offshore boundary and 10 m at the shoreline), medium: ~12 by 12 km (resolution between 200 m offshore and 80 m at the shoreline), and large: ~70 km alongshore by 15 (north end) to 30 (south end) km cross-shore (resolution between 500 m offshore and 200 m near the shoreline). The red circle indicates the directional wave buoy (550-m water depth) used to specify model boundary conditions.

Closer to shore, wave-induced pressure and velocity measurements were collected at 28 locations near La Jolla, CA on the 5.0-, 2.5-, and 1.0-m isobaths for 50 days in October and November 2003 (Fig. 1) (Thomson et al., 2006, 2007; Apotsos et al., 2008b). Current meters were located about 0.3 m above the seafloor, and pressure gages either were buried about 1.2 to 0.5 m below the bed (1.0 and 2.5 m depth, respectively) or were about 0.1 m above the bed (5.0 m depth). Data were collected at 2 or 16 Hz for 3072 s every hour. Data were discarded during low tides when current meters were not submerged and during periods when sensors were fouled or damaged (Elgar et al., 2005).

Nearshore bathymetry between the high-tide line and about 8-m water depth was measured approximately weekly using differential Global Positioning Systems mounted on waverunners, all-terrain vehicles, and pushcarts. Bathymetry was extended to the shelf break using swath sonar (2001) and National Ocean Service (1932–1972) depth soundings.

Significant wave heights at each sensor were estimated as 4 times the standard deviation of the sea-surface elevation fluctuations calculated from the time series of pressure (band pass filtered between 0.05 and 0.30 Hz) using linear wave theory and exponential decay of wave fluctuations through the sand bed (Raubenheimer et al., 1998). Wave directions relative to local shore normal (estimated from the 1.0- and 2.5-m isobaths) were calculated from the colocated pressure and velocity observations (Kuik et al., 1988). Owing to the curvature of the coast, the orientation of shore normal varied by 13° (Fig. 1). Mean wave directions, centroidal wave periods (defined as the inverse of the energy-weighted mean frequency), and radiation stresses were calculated from band-passed ($0.05 \le f \le 0.30$ Hz, where f is frequency) frequency-directional spectra.

In 550-m water depth, incident significant wave heights ranged from 0.40 to 1.75 m, mean wave directions ranged from 210° to 290° from north, and centroidal wave periods ranged from 5 to 14 s. Along the 2.5-m isobath wave heights ranged from 0.19 to 1.75 m, wave directions ranged from −18° to 15° relative to local shore normal, and centroidal periods ranged from 4.5 to 12 s.

3. Model

SWAN (Booij et al., 1999) is an Eulerian, phase-averaged, refraction wave model that simulates the evolution of the wave spectrum $E(\sigma, \theta)$ according to:

$$\frac{\partial N}{\partial t} + \frac{\partial (c_x N)}{\partial x} + \frac{\partial \left(c_y N\right)}{\partial y} + \frac{\partial (c_\sigma N)}{\partial \sigma} + \frac{\partial (c_\theta N)}{\partial \theta} = \frac{S}{\sigma} \quad (1)$$

where the action density $N(\sigma, \theta) = E(\sigma, \theta)/\sigma$, t is time, x and y are the cross- and alongshore coordinates, respectively, σ is the wave radian frequency, θ is the wave direction, and c_x, c_y, c_σ, and c_θ are the wave

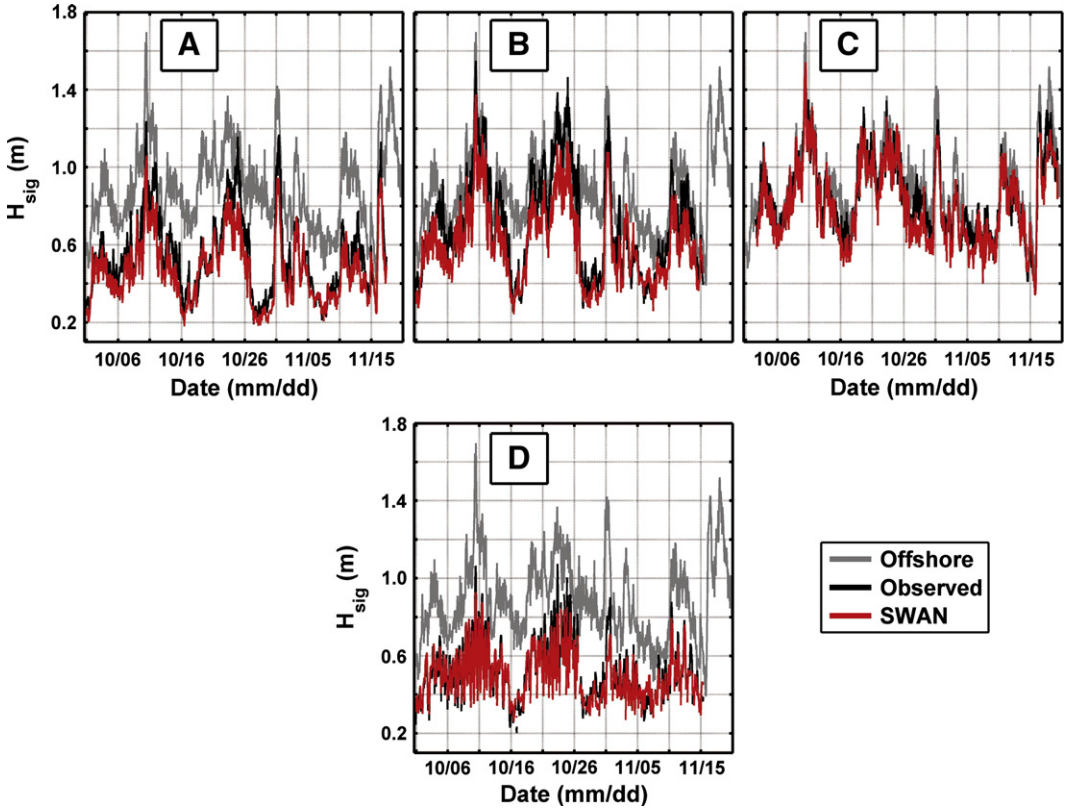

Fig. 3. Modeled (red curves) and observed (black curves) significant wave heights H_{sig}, versus time for (A–C) the 2.5 m isobath at alongshore distances of (A) 1240, (B) 1390, and (C) 2940 m, and (D) the 1.0-m isobath at an alongshore distance of 1390 m. The gray curve in all panels is H_{sig} observed in 550-m water depth.

group velocities in x, y, σ, and θ space, respectively. The source and sink term S is:

$$S = S_{in} + S_{nl} + S_{ds} \tag{2}$$

where S_{in} is wave generation via wind, S_{nl} includes parameterized triad and quartet nonlinear interactions, and S_{ds} is energy dissipation, including white capping, bottom friction, and wave breaking.

SWAN was run in stationary mode ($\partial N/\partial t = 0$ in Eq. (1)), in which waves are assumed to propagate instantaneously throughout the model domain. This assumption is reasonable for the small domain and slowly varying forcing considered here, and enables computationally efficient simulations with high grid resolutions. Wave generation and white-capping were negligible because wind speeds were less than 5 m/s. Nonlinear triad interactions (Freilich and Guza, 1984; Elgar and Guza, 1985b) are significantly larger than quartet interactions for the short spatial scales and shallow depths considered here, and thus quartet interactions were neglected. The model runs included the SWAN default (JONSWAP) expression for bottom friction dissipation (Hasselmann et al., 1973) using a coefficient of 0.067 m^2/s^3. Bottom dissipation is small for these short propagation distances. Breaking wave dissipation was estimated with a bore-based model (Battjes and Janssen, 1978), with the depth-induced wave breaking parameter $\gamma = 0.5$ based on fitting to 5 days of observations. This value for γ is within the range ($0.2 \le \gamma \le 0.8$) used in prior studies on natural beaches (Apotsos et al., 2008b, and references therein). The frequency and directional resolution were defined using the SWAN default values, resulting in 24 logarithmically-distributed frequency bins (e.g., $\Delta f \approx 0.14f$ (Booij et al., 2004)) over $0.05 \le f \le 1.00$ Hz and 36 10° directional bins evenly spaced over $0° \le \theta \le 360°$.

SWAN simulations used three nested curvilinear grids (Fig. 2). The largest-area grid, which improved the model skill for waves arriving from the south, was initialized on the three open boundaries with observations from the buoy in 550-m water depth, 11 km offshore of the study site (Fig. 2). The boundary conditions on the small and medium grids were determined from computations over the medium and large grids, respectively. Simulations suggest negligible errors in the small and medium area grids resulted from the assumption of uniform waves on the north and south cross-shore open water boundaries on the large grid.

Offshore buoy observations from October 1 to November 20, 2003 yielded 1223 hourly model predictions of wave frequency-directional spectra at the 28 instrument locations (Fig. 1). Significant wave height H_{sig}, mean wave direction (relative to shore normal) θ, centroidal wave period T, and alongshore wave radiation stress S_{xy} were computed from the low-passed ($0.05 \le f \le 0.30$ Hz) output spectra, and are compared with the observations.

4. Model-data comparisons

SWAN predicts the observed wave heights, H_{sig}, accurately in all depths (Fig. 3, compare red with black curves), with root-mean-square (RMS) differences of about 0.13 m and high correlations ($r^2 > 0.8$, where $r^2 = cov^2(x,y)/[var(x)var(y)]$, cov($x$,$y$) is the covariance between x and y, var(x) and var(y) are the variances of x and y, and x and y are the observed and predicted parameters) between model predictions and observations (Table 1). Far from the canyon, observed and predicted H_{sig} in 2.5-m water depth are similar to H_{sig} in 550-m depth (Fig. 3C, compare red and black curves with gray curve). In contrast, near the canyon, observed and predicted H_{sig} in 2.5-m water depth are significantly smaller (as much as a factor of 4) than observed offshore (Fig. 3A). Owing to depth-limited wave breaking, observed and predicted H_{sig} in 1.0-m water depth are smaller than in 2.5-m water depth, especially at low tide (Fig. 3D).

Table 1
Root-mean-square (RMS) errors, biases, and r^2 between model predictions and observations of significant wave height (H_{sig}, cm), mean wave direction (θ, degrees), centroidal wave period (T, seconds), and radiation stress (S_{xy}/ρ, m^3/s^2) as a function of water depth (m) and distance (m) for all instrument locations. RMS errors are calculated after biases are removed. Mean values averaged over all sensor locations are given at the bottom of the table.

Depth	X	H_{sig} RMS, Bias, r^2	θ RMS, Bias, r^2	T RMS, Bias, r^2	S_{xy}/ρ RMS, Bias, r^2
5.0	1390	0.13, −0.11, 0.84	2.2, 0.7, 0.70	0.6, −0.3, 0.79	0.02, 0.012, 0.56
	1550	0.11, 0.02, 0.83	2.7, 2.9, 0.75	0.6, 0.1, 0.86	0.03, −0.001, 0.72
	1700	0.10, −0.06, 0.86	2.6, 2.1, 0.80	0.5, 0.3, 0.90	0.04, 0.009, 0.72
	2150	0.09, 0.02, 0.84	2.4, 3.2, 0.76	0.6, 0.5, 0.89	0.03, 0.006, 0.71
	2310	0.11, 0.03, 0.79	2.2, 2.3, 0.74	0.6, 0.4, 0.89	0.03, 0.006, 0.64
	2560	0.09, −0.01, 0.86	1.9, 1.5, 0.75	0.6, 0.4, 0.88	0.02, 0.002, 0.61
	2670	0.07, 0.01, 0.87	1.9, 0.6, 0.82	0.4, 0.1, 0.96	0.02, 0.001, 0.72
	2940	0.09, −0.01 0.85	1.8, 1.2, 0.74	0.5, 0.2, 0.89	0.02, 0.001, 0.50
2.5	340	0.08, −0.01 0.90	2.4, −2.2, 0.42	0.5, 0.3, 0.84	0.01, 0.001, 0.65
	910	0.06, −0.05 0.90	1.8, 0.6, 0.45	0.4, 0.2, 0.83	0.01, −0.004, 0.04
	1240	0.08, −0.07, 0.86	1.3, 1.9, 0.49	0.6, 0.2, 0.65	0.01, −0.001, 0.30
	1390	0.11, −0.10, 0.84	1.5, 5.2, 0.58	0.6, 0.1, 0.72	0.01, 0.003, 0.24
	1550	0.09, −0.01, 0.85	1.6, 2.7, 0.74	0.6, 0.5, 0.76	0.02, 0.001, 0.76
	1700	0.10, −0.07, 0.83	3.5, −1.3, 0.29	0.7, 0.9, 0.75	0.04, 0.011, 0.60
	2150	0.09, 0.02, 0.77	2.3, −2.9, 0.52	0.8, 1.1, 0.75	0.02, −0.012, 0.68
	2310	0.08, −0.01, 0.82	2.2, −1.7, 0.50	0.7, 0.9, 0.79	0.02, −0.002, 0.56
	2560	0.09, −0.04, 0.85	1.7, −1.2, 0.67	0.7, 0.8, 0.76	0.02, −0.007, 0.65
	2670	0.08, −0.02, 0.85	1.7, −1.5, 0.61	0.7, 0.6, 0.77	0.01, −0.001, 0.34
	2940	0.08, −0.04, 0.85	1.4, −2.1, 0.65	0.7, 0.5, 0.76	0.01, −0.001, 0.38
1.0	1240	0.06, 0.01, 0.79	1.7, 1.3, 0.19	0.7, −0.3, 0.40	0.01, −0.001, 0.11
	1390	0.06, −0.02, 0.84	2.1, −1.5, 0.20	0.6, −0.1, 0.62	0.01, −0.006, 0.08
	1550	0.06, −0.02, 0.84	2.6, −0.5, 0.37	0.9, 0.1, 0.26	0.01, −0.001, 0.65
	1700	0.07, 0.07, 0.83	4.5, 0.2, 0.08	1.0, 0.6, 0.23	0.01, −0.009, 0.42
	2150	0.08, 0.04, 0.77	2.5, −0.7, 0.41	0.9, 0.8, 0.47	0.02, −0.12, 0.58
	2310	0.07, 0.12, 0.79	3.1, −3.4, 0.25	0.9, 0.3, 0.43	0.02, −0.14, 0.37
	2560	0.06, 0.07, 0.83	2.5, −0.8, 0.21	0.8, 0.2, 0.57	0.01, −0.009, 0.32
	2670	0.07, 0.07, 0.79	2.9, −2.2, 0.13	0.8, 0.3, 0.62	0.02, −0.016, 0.20
	2940	0.06, 0.08, 0.82	2.1, −0.5, 0.24	0.9, 0.1, 0.43	0.01, −0.007, 0.15
Mean		0.08, 0.00, 0.83	2.3, 0.1, 0.50	0.7, 0.4, 0.70	0.02, −0.010, 0.47

Observed wave directions relative to shore normal, θ, are predicted well (Fig. 4, compare red with black curves), with RMS errors less than 3° (Table 1). Away from the canyon influence, the observed and predicted θ in 2.5-m water depth are correlated with θ offshore (Fig. 4C, compare red and black curves with the gray curve). Nearer the canyon, directions in 2.5-m depth can differ significantly from those offshore (Fig. 4A and B). Wave directions in 2.5-m water depth near and far from the canyon can have opposite signs. For example, on 10/02, 10/18, and 11/03 far from the canyon observed and predicted $\theta<0$ (waves approach from the south, Fig. 4C), whereas near the canyon $\theta>0$ (waves approach from the north, Fig. 4B). Although RMS differences between modeled and observed directions are small, the correlation between modeled and observed directions decreases as the depth decreases (Table 1) because refraction greatly reduces the range of wave directions about shore normal (compare Fig. 4B with D).

The alongshore gradients in wave height (Fig. 3) and direction (Fig. 4) create alongshore gradients in wave-driven setup and radiation stress (Fig. 5) that drives complex surfzone circulation (Apotsos et al., 2008b). The observed alongshore variations in wave height (up to a factor of 4 over less than 1000 m) are strongest for southerly swell, and are predicted accurately by the model, as are the corresponding radiation stresses (Fig. 5A). Observed and predicted radiation stresses S_{xy} are near zero near the canyon, and become increasingly negative with distance from the canyon before decreasing toward zero far from the canyon (Fig. 5A). Refraction by the canyons and changes in shoreline orientation cause alongshore variation in the wave direction relative to the local shore normal. For example, with offshore waves from the west (Fig. 4), the direction relative to shore normal of incident waves and the associated radiation stresses changed sign over less than 500 m alongshore in shallow water (Fig. 5B), possibly resulting in strong converging flows. Alongshore variations of wave height and radiation stresses are similar in 2.5- and 5.0-m water depths (Fig. 5), and are predicted accurately by the model. Reduced correlation between modeled and observed S_{xy} in shallow water (Table 1) primarily is owing to the reduced range in directions (and thus in S_{xy}) over which the correlation is calculated as the depth decreases.

Centroidal wave periods (T) also are predicted well (Fig. 6). In 2.5-m water depth, observed and predicted T increase with distance from the canyon, especially for the long period ($T>10$ s) incident waves most affected by the canyon. For example, on 10/28 the canyon blocked 14 s swell incident from the south (gray curve in Fig. 4), and significantly reduced H_{sig} (Fig. 3) and T (Fig. 6) near the canyon. In contrast, on 11/15 shorter period sea (Fig. 6) from the west (Fig. 4) was not strongly affected by the canyon. Both cases are predicted well.

Although SWAN predicts T well, with RMS differences less than 1.0 s and biases less than 1.4 s (Table 1), the errors increase as the depth decreases (Table 1), possibly because nonlinear energy transfers are not modeled accurately. On 10/20 and 10/27 the primary peak (roughly $0.05\leq f\leq 0.10$ Hz) of the wave energy density spectrum is predicted well (Fig. 7), and H_{sig} is modeled accurately (Fig. 3). However, the energy levels of all harmonics are under-predicted on 10/20 (Fig. 7A), and only the first harmonic ($f=0.12$ Hz) is predicted well on 10/27 (Fig. 7B), resulting in over-prediction of the centroidal period (Fig. 6C). The nonlinear transfers of energy from swell to higher frequency motions are not modeled accurately because self–self triad interactions (e.g., interactions between waves with frequencies 0.06, 0.06, and 0.12 Hz) are parameterized crudely, and interactions between waves with three different frequencies (e.g., 0.06, 0.12, and 0.18 Hz, or 0.06, 0.07, and 0.13 Hz) are not included.

5. Conclusions

The SWAN numerical wave model accurately predicts the observed evolution of surface gravity waves propagating 11 km from 550-m water depth to the shoreline over complicated nearshore bathymetry that

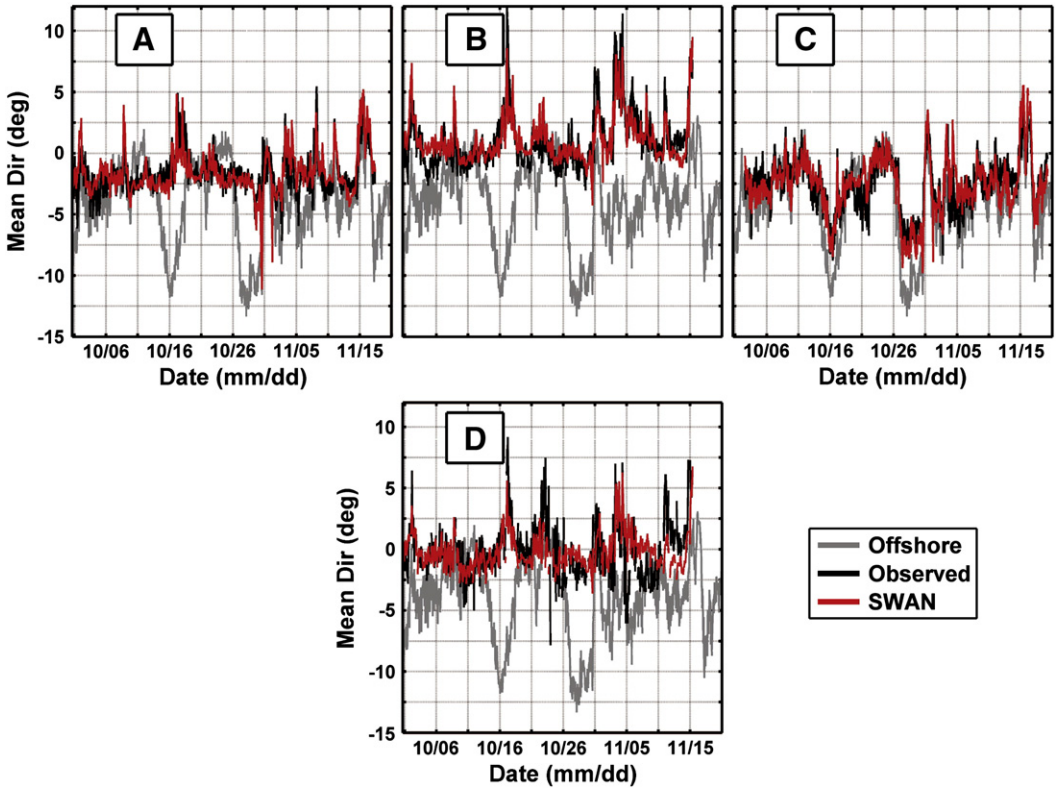

Fig. 4. Modeled (red curves) and observed (black curves) centroidal wave directions relative to local shore normal (positive values represent waves from north of shore normal) versus time for (A–C) the 2.5 m isobath at alongshore distances of (A) 1240, (B) 1390, and (C) 2940 m, and (D) the 1.0-m isobath at an alongshore distance of 1390 m. The gray curve in all panels is the mean wave direction observed in 550-m water depth scaled by a factor of 0.2. A bias, usually less than 3° but as large as 5.2° (see Table 1), which may be owing to instrument alignment errors, has been removed from the data.

includes a steep submarine canyon. Although SWAN does not model accurately the nonlinear energy transfers that result in harmonic growth and changing wave shapes in shallow water, the root-mean-square errors of the predicted wave heights, mean directions, centroidal periods, and radiation stresses in 5.0-, 2.5-, and 1.0-m water depths are less than 0.13 m, 5°, 1 s, and 0.05 m^3/s^2 respectively. The observed strong alongshore variations in wave height and direction (and thus radiation stresses) in 5.0- and 2.5-m water depths also are predicted well.

Acknowledgements

Staff from the PVLAB (Woods Hole Oceanographic Institution) and the Center for Coastal Studies (Scripps Institution of Oceanography) are thanked for their efforts in obtaining the observations. Bill O'Reilly made many valuable suggestions. Funding was provided by the Office of Naval Research, the National Science Foundation, and a National Security Science and Engineering Faculty Fellowship.

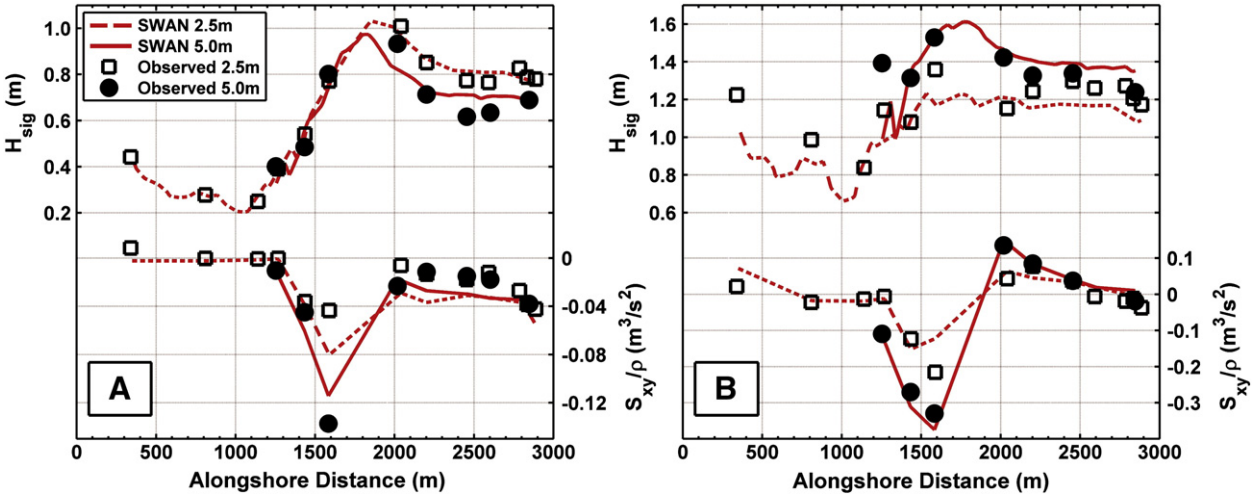

Fig. 5. Modeled (curves) and observed (symbols) significant wave heights H_{sig} (left vertical axis) and radiation stresses S_{xy} (right vertical axis) on the 5.0- (solid curves and filled circles) and 2.5-m (dashed curves and open squares) isobaths versus alongshore distance for (A) 10/28/2003 at 14:00 PST (offshore wave conditions were $H_{sig}=0.92$ m, $\theta=214°$, and $T=13$ s, and (B) 10/10/2003 at 13:00 PST (offshore wave conditions were $H_{sig}=1.39$ m, $\theta=265°$, and $T=9.6$ s). A bias in wave direction, which may be owing to instrument alignment errors, has been removed before computing S_{xy}.

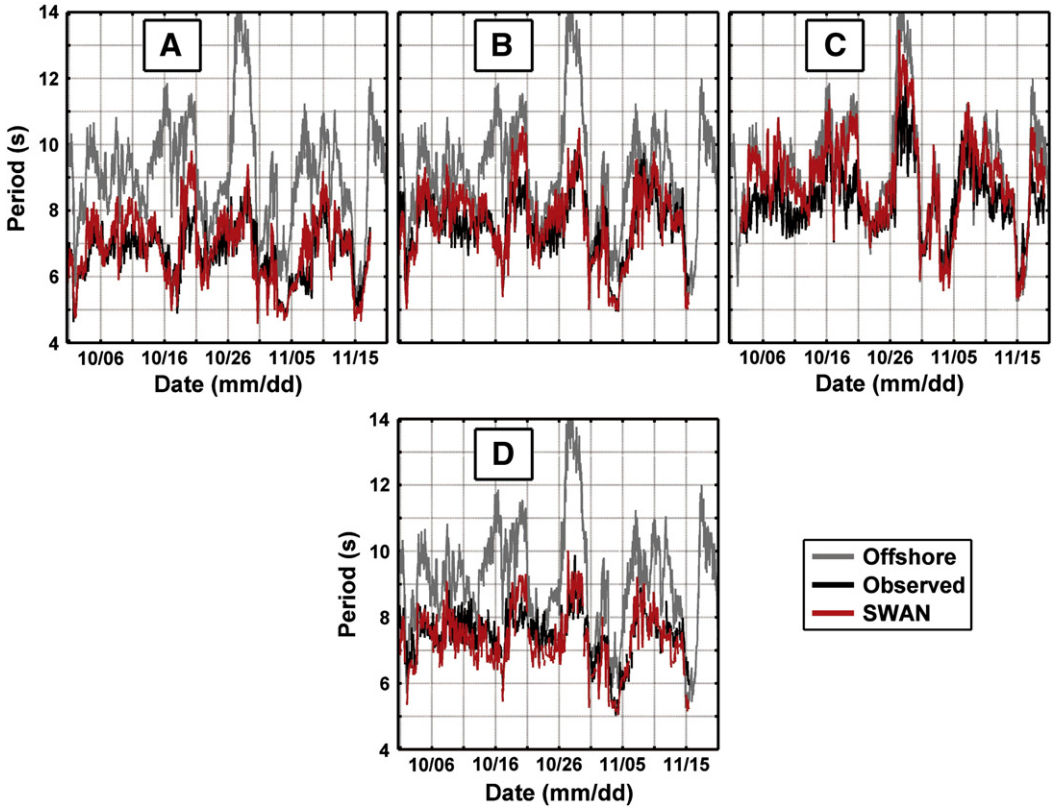

Fig. 6. Modeled (red curves) and observed (black curves) centroidal wave periods versus time for (A–C) the 2.5 m isobath at alongshore distances of (A) 1240, (B) 1390, and (C) 2940 m, and (D) the 1.0-m isobath at an alongshore distance of 1390 m. The gray curve in all panels is the centroidal wave period observed in 550-m water depth.

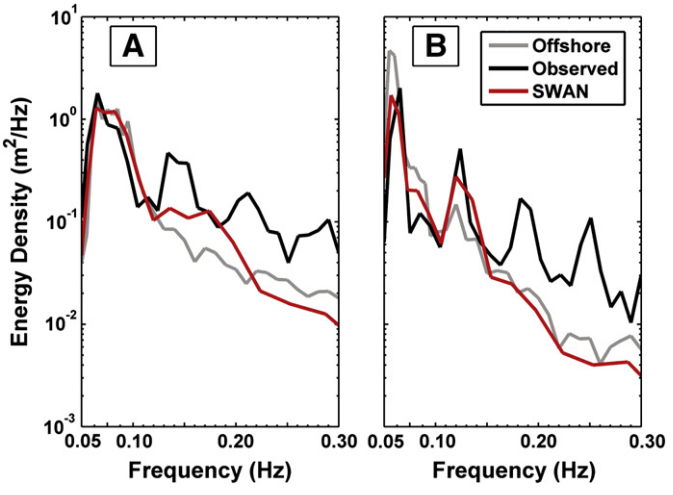

Fig. 7. Modeled (red curves) and observed (black curves) energy density versus frequency in 2.5 m water depth at an alongshore distance of 2940 m on (A) 10/20/2003 at 09:00 PST (offshore wave conditions were $H_{sig}=0.96$ m, $\theta=266°$, and $T=11$ s) and (B) 10/27/2003 at 16:00 PST (offshore wave conditions were $H_{sig}=1.01$ m, $\theta=211°$, and $T=14$ s). The gray curves are the energy density spectra estimated from observations in 550-m water depth.

References

Apotsos, A., Raubenheimer, B., Elgar, S., Guza, R., 2008a. Testing and calibrating parametric wave transformation models on natural beaches. Coastal Eng. 55, 224–235.

Apotsos, A., Raubenheimer, B., Elgar, S., Guza, R., 2008b. Wave-driven setup and alongshore flows observed onshore of a submarine canyon. J. Geophys. Res. 113, C07025. doi:10.1029/2007JC004514.

Battjes, J., Janssen, J., 1978. Energy loss and set-up due to breaking of random waves. Proceedings of 16th International Conference on Coastal Engineering, pp. 569–587.

Battjes, J., Stive, M., 1985. Calibration and verification of a dissipation model for random breaking waves. J. Geophys. Res. 90, 9159–9167.

Booij, N., Ris, R., Holthuijsen, L., 1999. A third-generation wave model for coastal regions, 1, model description and validation. J. Geophys. Res. 104, 7649–7666.

Booij, N., Haagsma, I.J., Holthuijsen, L., Keiftenburg, A., Ris, R., van der Westhuysen, A., Zijlema, M., 2004. SWAN Cycle-III version 40.41 User Manual. 39 pp.

Chawla, A., Ozkan-Haller, H., Kirby, J., 1998. Spectral model for wave transformation and breaking over irregular bathymetry. J. Waterw. Port Coast. Ocean Eng. 124, 189–198.

Chen, Y., Guza, R., Elgar, S., 1997. Modeling breaking surface waves in shallow water. J. Geophys. Res. 102, 25,035–25,046.

Dalrymple, R., Kirby, J., Hwang, P., 1984. Wave diffraction due to areas of energy dissipation. J. Waterw. Port Coast. Ocean Eng. 110, 67–79.

Elgar, S., Guza, R., 1985a. Shoaling gravity waves: comparisons between field observations, linear theory and a nonlinear model. J. Fluid Mech. 158, 44–70.

Elgar, S., Guza, R., 1985b. Observations of bispectra of shoaling surface gravity waves. J. Fluid Mech. 161, 425–448.

Elgar, S., Freilich, M., Guza, R., 1990. Model-data comparisons of moments of nonbreaking shoaling surface gravity waves. J. Geophys. Res. 95, 16,055–16,063.

Elgar, S., Raubenheimer, B., Guza, R.T., 2005. Quality control of acoustic Doppler velocimeter data in the surfzone. Meas. Sci. Technol. 16, 1889–1893.

Freilich, M., Guza, R., 1984. Nonlinear effects on shoaling surface gravity waves. Phil. Trans. R. Soc. Lond. A 311, 1–41.

Hasselmann, K., et al., 1973. Measurements of wind-wave growth and swell decay during the Joint North Sea Wave Project (JONSWAP). Dtsch. Hydrogr. Z. Suppl. 12 (A8), 1–95.

Herbers, T., Burton, M., 1997. Nonlinear shoaling of directionally spread waves on a beach. J. Geophys. Res. 102, 21,101–21,114.

Kaihatu, J., Kirby, J., 1995. Nonlinear transformation of waves in finite water depth. Phys. Fluids 7, 1903–1914.

Kirby, J., Dalrymple, R., 1994. Combined Refraction/Diffraction Model—REF/DIF 1, Version 2.5, Center for Applied Coastal Research, Res. Rpt. CACR-94-22.

Kuik, A., van Vledder, G., Holthuijsen, L., 1988. A method for routine analysis of pitch-and-roll buoy data. J. Phys. Oceanogr. 18, 1020–1034.

Le Méhauté, B., Wang, J., 1982. Wave spectrum changes on a sloped beach. J. Waterw. Port Coast. Ocean Eng. 108, 33–47.

Lippmann, T., Holman, R., 1990. The spatial and temporal variability of sand bar morphology. J. Geophys. Res. 95, 11,575–11,590.

Liu, P., Yoon, S., Kirby, J., 1985. Nonlinear refraction–diffraction of waves in shallow water. J. Fluid Mech. 153, 185–201.

Long, J., Özkan-Haller, H., 2005. Offshore controls on nearshore rip currents. J. Geophys. Res. 110, C12007. doi:10.1029/2005JC003018.

Longuet-Higgins, M., 1957. On the transformation of a continuous spectrum by refraction. Proc. Camb. Phil. Soc. 53, 226–229.
MacMahan, J., Thornton, E., Reniers, A., 2006. Rip current review. Coastal Eng. 53, 191–208. doi:10.1016/j.coastaleng.2005.10.009.
Madsen, P., Sorensen, O., 1992. A new form of the Boussinesq equations with improved linear dispersion characteristics. Part 2. A slowly varying bathymetry. Coastal Eng. 18, 183–204.
Madsen, P., Warren, I., 1984. Performance of a numerical short-wave model. Coastal Eng. 8, 73–93.
Madsen, P., Murray, R., Sorensen, O., 1991. A new form of the Boussinesq equations with improved linear dispersion characteristics. Coastal Eng. 15, 371–388.
Magne, R., Belibassakis, K., Herbers, T., Ardhuin, F., O'Reilly, W., Rey, V., 2007. Evolution of surface gravity waves over a submarine canyon. J. Geophys. Res. 112, C01002. doi:10.1029/2005JC003035.
Mase, H., Kirby, J., 1992. Hybrid frequency-domain KdV equation for random wave transformation. Proc. 23rd Int. Conf. on Coastal Eng, pp. 474–487.
Mei, C.C., 1989. The Applied Dynamics of Ocean Surface Waves. World Scientific, Singapore.
Norheim, C., Herbers, T., Elgar, S., 1998. Nonlinear evolution of surface wave spectra on a beach. J. Phys. Oceanogr. 28, 1534–1551.
O'Reilly, W., Guza, R., 1991. Comparison of spectral refraction and refraction diffraction wave models. J. Waterw. Port Coast. Ocean Eng. 117, 199–215.
Panchang, V., Pearce, B., Ge, W., Cushman-Rosin, B., 1991. Solution of the mild-slope wave problem by iteration. Appl. Ocean Res. 13, 187–199.
Peregrine, H., 1967. Long waves on a beach. J. Fluid Mech. 27, 815–827.
Raubenheimer, B., Elgar, S., Guza, R., 1998. Estimating wave heights from pressure measured in a sand bed. J. Waterw. Port Coast. Ocean Eng. 124, 151–154.
Ris, R., Holthuijsen, L., Booij, N., 1999. A third-generation wave model for coastal regions, 2, verification. J. Geophys. Res. 104, 7667–7681.
Rogers, W., Kaihatu, J., Hsu, L., Jensen, R., Dykes, J., Holland, K., 2007. Forecasting and hindcasting waves in the SWAN model in the Southern California Bight. Coastal Eng. 54, 1–15.
Schaffer, H., Madsen, P., Deigaard, R., 1993. A Boussinesq model for waves breaking in shallow water. Coastal Eng. 20, 185–202.
Thomson, J., Elgar, S., Herbers, T., Raubenheimer, B., Guza, R., 2006. Tidal modulation of infragravity waves via nonlinear energy losses in the surfzone. Geophys. Res. Lett. 33, L05601. doi:10.1029/2005GL025514.
Thomson, J., Elgar, S., Herbers, T., Raubenheimer, B., Guza, R., 2007. Refraction and reflection of infagravity waves near submarine canyons. J. Geophys. Res. 112, C10009. doi:10.1029/2007JC004227.
Thornton, E., Guza, R., 1983. Transformation of wave height distribution. J. Geophys. Res. 8, 5925–5938.
Zubier, K., Panchang, V., Demirbilek, Z., 2003. Simulation of waves at Duck (North Carolina) using two numerical models. Coast. Eng. J. 45 (3), 439–469.